THE JOURNAL OF
PHYSICAL CHEMISTRY C

pubs.acs.org/JPCC

Article

Controlling Particle Size and Phase Purity of “Single-Crystal” $LiNi_{0.5}Mn_{1.5}O_4$ in Molten-Salt-Assisted Synthesis

Wei-Na Wang,[#] Dechao Meng,[#] Guannan Qian, Sijie Xie, Yanbin Shen, Liwei Chen, Xiaomin Li, Qunli Rao, Haiying Che, Jiabing Liu, Yu-Shi He, Zi-Feng Ma, and Linsen Li*

Cite This: *J. Phys. Chem. C* 2020, 124, 27937−27945

Read Online

ACCESS | Metrics & More | Article Recommendations | Supporting Information

ABSTRACT: Spinel-structured lithium nickel manganese oxide ($LiNi_{0.5}Mn_{1.5}O_4$, LNMO) is a low-cost battery cathode material with a high operating voltage (∼4.7 V vs Li^+/Li), relatively high capacity (∼147 mA h g^{-1}), and good rate performance. Previous studies have suggested that large particle size, single-crystal-like morphology, and high phase purity are favorable for achieving good electrochemical performance. However, simultaneous control over these properties is difficult for conventional solid-state synthesis at high temperatures. Here, we report a molten-salt-assisted method to prepare large-size (median grain size D_{50} = 16.8 μm) single-crystal LNMO with molten lithium molybdate (Li_2MoO_4) serving as the medium of ion diffusion and crystal growth. *In situ* X-ray diffraction (XRD) studies of the material preparation process reveal structural disorder and formation of the rock-salt impurity phase at high temperatures, which are reverted upon cooling. The correlations between the cooling rate and structural ordering/phase purity at the single-particle level are further studied using correlative scanning electron microscopy and Raman spectroscopy (SEM-Raman) techniques. SEM-Raman studies for the first time reveal that the Ni-rich rock-salt impurity phase actually exists at the interior of the large-size LNMO particles, which is difficult to be detected by conventional XRD or Raman spectroscopy because of limitations in probing depth. We further confirm that slow cooling is the key to increasing structural ordering and enhancing electrochemical performance of LNMO. The optimized LNMO sample shows excellent cycle performance by retaining ∼85% initial capacity after 300 charge−discharge cycles and acceptable level of rate capability despite its large particle size. Our results highlight the importance of mechanistic studies into material synthesis, which provide the basis for designing better materials and more efficient preparation methods.

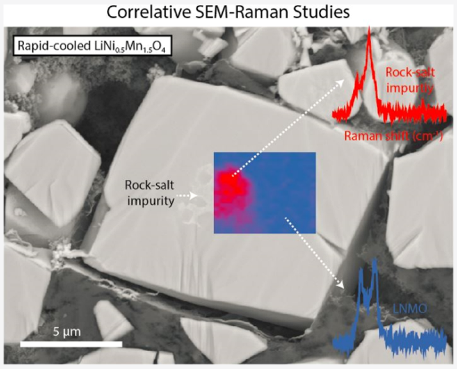

■ INTRODUCTION

Lithium-ion batteries play an increasingly important role in the new era of clean electrification.[1] In existing batteries, Co-containing cathode materials such as $LiCoO_2$ (LCO), $LiNi_xCo_yMn_zO_2$ (NMC, $x + y + z = 1$), and $LiNi_{0.8}Co_{0.15}Co_{0.05}O_2$ (NCA) are widely used.[2] In the last few years, we have witnessed a surge in demand for Co and dramatic fluctuation in its price (∼30,000−70,000 \$ ton^{-1}). Because Co is much more expensive than Ni (∼13,000 \$ ton^{-1}) and Mn (∼2000 \$ ton^{-1}) and a large portion of the Co-mining comes from the geopolitically unstable central African countries, there is a growing concern over Co supply chain from both the battery manufacturing industry and end consumers. To develop sustainable batteries, it is necessary to reduce our reliance on Co.[3−8] One promising alternative is the spinel-structured $LiNi_{0.5}Mn_{1.5}O_4$ (LNMO), which is a low-cost cathode material with a high operating voltage (∼4.7 V vs Li^+/Li), relatively high capacity (∼147 mA h g^{-1}), and good rate performance.[9−23]

“Single-crystal” cathode materials have attracted significant research attention recently because of their excellent cycle performance.[24−27] Here, “single-crystal” means that each particle is made up of just one or several micron-sized crystallites. This nomenclature is chosen to contrast with the case of polycrystalline cathode materials, in which each particle is made of many nanoscale crystallites. LNMO has anisotropic Vegard coefficients—its lattice changes anisotropically during lithium extraction and insertion.[28] For this reason, polycrystalline LNMO particles are intrinsically vulnerable to grain-boundary fracture, which leads to dramatic increase in surface area and aggravates various surface-related degradation mechanisms such as electrolyte decomposition, metal dissolution, and surface structural reconstruction. For the LNMO cathode, it is favorable to have a small surface area and maintain it that way during cycling. This is perhaps more

Received: October 14, 2020
Revised: December 6, 2020
Published: December 15, 2020

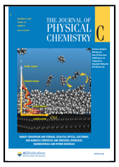

https://dx.doi.org/10.1021/acs.jpcc.0c09313
J. Phys. Chem. C 2020, 124, 27937−27945

important to LNMO than other cathode materials because its high operating voltage poses a major challenge to common liquid electrolytes.[12] Based on previous studies,[28] we expect that large-size (i.e., small surface area) and fracture-resistant (i.e., no surface area increase) single-crystal LNMO particles can enable stable cycle performance. However, there are no preparation methods available for single-crystal LNMO particles with median grain size (D_{50}) greater than 10 μm, which is a typical size for commercial LCO, NMC, and NCA cathode materials and a key to achieving high volumetric energy density.

Synthesis of LNMO is facing another unique challenge in controlling the phase purity. Unlike other cathode materials (LCO, NMC, NCA, Li_2MnO_4, or $LiFePO_4$) normally prepared as a single phase, LNMO can crystallize into two different phases with either a cation-ordered ($P4_332$) Ni/Mn arrangement or a disordered ($Fd\bar{3}m$) one with oxygen deficiency (i.e., $LiNi_{0.5}Mn_{1.5}O_{4-\delta}$).[9,20,21,29,30] Impurity phases such as rock-salt-structured $Li_xNi_{1-x}O$ are also commonly observed.[14,20,30] It has been found that the ordered $P4_332$ phase starts to lose lattice oxygen at a temperature above 750 °C and hence the disordered $Fd\bar{3}m$ phase and the rock-salt impurity phase are produced.[19] This process is largely reversible—structural ordering and stoichiometry can be recovered with oxygen uptake upon cooling. Electrochemical measurements[14] and neutron diffraction[19] made on bulk samples indicate that slow cooling favors the formation of the ordered phase. However, because of the lack of suitable characterization techniques, the disorder-order transition at the single-particle level during cooling and its correlation with cooling rate has not been fully understood. It is also unclear where the rock-salt impurity phase is and how it is formed and transforms during the preparation process of LNMO. We suggest that correlative scanning electron microscopy and Raman spectroscopy (SEM-Raman), a powerful combination providing high-resolution morphological, structural, and chemical information can meet the challenge. This technique has been applied to study two-dimensional materials[31] and minerals.[32] However, to the best of our knowledge, it has not been applied to study LNMO (or any battery materials) and its preparation process.

Here, we show that single-crystal LNMO particles with large size (D_{50} = 16.8 μm) can be synthesized in molten Li_2MoO_4. We choose Li_2MoO_4 as the flux because of its low melting point (705 °C) and high solubility in water (~45 g/100 mL H_2O at 25 °C). It provides the medium for ion diffusion and crystal growth at the synthesis temperature (950 °C) and can be conveniently separated from the product by water washing. The Li_2MoO_4 flux has been previously used to grow Li_2MSiO_4 (M = Mg or Zn),[33] $LiNi_{1/3}Co_{1/3}Mn_{1/3}O_2$,[34] and $LiIn_2SbO_6$,[35] and other materials. The preparation process of LNMO was investigated by *in situ* X-ray diffraction (XRD), which revealed concurrent formation of disordered spinel LNMO and rock-salt impurity phases under the isothermal annealing condition at high temperature used for the synthesis. We further studied the process of the rock-salt impurity phases reverting back to the spinel phases at the single-particle level at different cooling rates through correlative SEM-Raman and revealed the correlations between structure and electrochemical performance. The slow-cooled, large-size single-crystal LNMO sample with little rock-salt impurity exhibited remarkable cycle performance by retaining ~85% of initial capacity after 300 charge−discharge cycles and good rate capability.

■ METHODS

Synthesis of LNMO Samples. 0.01 mol of $Ni(OH)_2$ and 0.03 mol of MnO_2 were manually mixed with 0.02 mol of LiOH and 0.005 mol of Li_2MoO_4 in an agate mortar and then transferred into an alumina crucible. The crucible was covered by a lid to allow air intake during the synthesis but avoid excess evaporation of Li salts. The material mixture was heated to 950 °C at a rate of 3 °C min^{-1} and held at 950 °C for 8 h in air before cooling at different rates to get LNMO samples S1, S2, and S3, respectively. The obtained powders were recovered from the crucible, ground in the agate mortar, and washed using deionized water to separate the material from the water-soluble Li-salts. The LNMO powders were collected by centrifugation and dried at 80 °C in air. The material was ground again to pass through a 400-mesh sieve and then stored in a humidity-controlled storage chamber (relative humidity $\leq$ 25%) before further tests.

Material Characterizations. The particle morphologies were investigated using a scanning electron microscope (SEM, Phenom Pro). The phase identification was analyzed with a Bruker D8 X-ray diffractometer (XRD) using Cu Kα radiation. *In situ* XRD was performed using an X-ray diffractometer (Bruker D8, Cu Kα radiation) equipped with a ceramic heating stage (Anton Paar). The precursors were mixed and pressed into a pellet. The pellet was loaded onto the ceramic stage and heated from room temperature to 900 °C at a ramping rate of ~2.5 °C min^{-1}. XRD patterns were collected continuously during the isothermal stage and cooling. Each XRD scan took ~10 min to finish. Particle size distribution was measured by a particle size analyzer (Mastersizer 2000, Malvern Panalytical). Ion milling was performed using an ion-beam milling system (Leica EM TIC 3X). SEM-Raman experiments were performed using a TESCAN MAIA3 electron microscope integrated with a WITec apyron confocal Raman imaging system. The Raman spectra were recorded in the region of 0−1800 cm^{-1} using 532 nm laser at a power of 2 mW and 1200 line mm^{-1} grating. To obtain high-quality single-point spectrum with good signal-to-noise ratio, the laser beam was focused onto the smooth cross section of a single particle, and each single-point scan was measured five times with a total accumulation time of 100 s. For the Raman area maps, the Raman spectra were collected within a selected rectangular grid of 5 × 4 μm^2 in a stepwise manner. Data smoothing, normalization, fitting, and overlaying of the spectra were performed using the WITec Project 5 software. Energy-dispersive X-ray (EDX) line scan analysis was performed using the same SEM (Tescan MAIA3).

Electrochemical Testing. The LNMO samples were mixed with polyvinyl difluoride and super-P carbon black with a weight ratio of 90:5:5 in NMP using a Thinky Mixer (ARE-310). The slurries were coated onto aluminum foils using a film applicator. The electrodes were first dried in a convection oven at 80 °C for 3 h and then dried at 120 °C under vacuum for 10 h. A typical loading of the electrodes for half-cell tests is about 3−4 mg cm^{-2}. Half-cells were assembled using Li foil (0.45 mm in thickness) as the anode, a polyethylene separator, and 1 M $LiPF_6$ dissolved in ethylene carbonate-ethyl methyl carbonate (3:7 by weight) as the electrolyte in an argon-filled glovebox (Mikrona, O_2/H_2O < 0.1 ppm). Electrochemical cycling measurements were performed using battery cyclers (Neware BTS4000). The coin cells were cycled inside temperature chambers set at 30

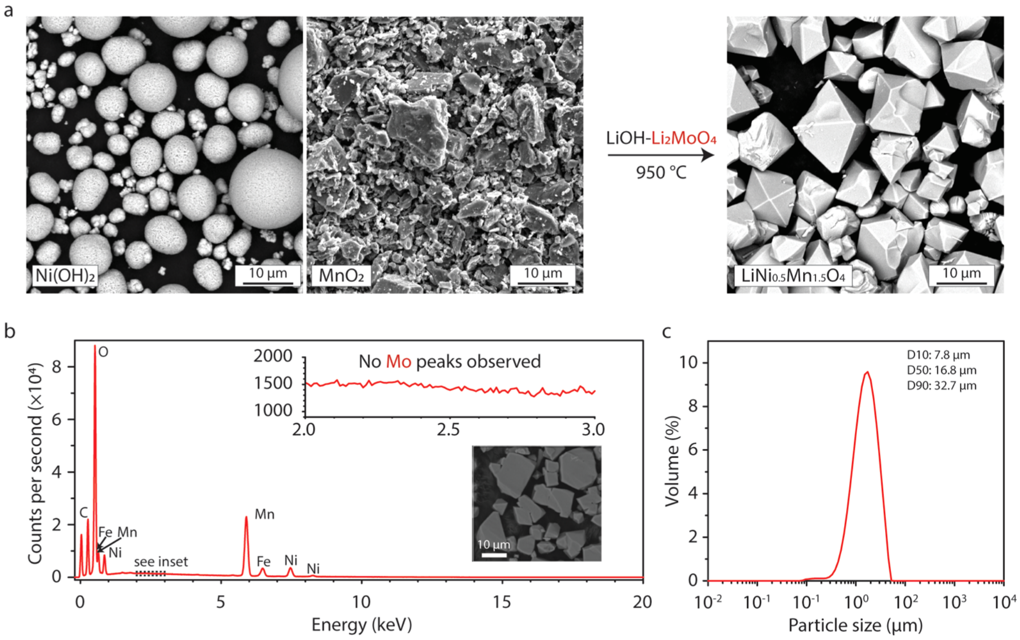

Figure 1. Preparation of large-size single-crystal $LiNi_{0.5}Mn_{1.5}O_4$ particles. (a) Synthesis process of large-size single-crystal $LiNi_{0.5}Mn_{1.5}O_4$ particles using LiOH, $Ni(OH)_2$, and MnO_2 as precursors and Li_2MoO_4 as the salt; (b) EDX spectrum collected from the LNMO sample. No Mo peaks could be detected. The EDX spectrum was collected from a 50 μm × 40 μm region as shown in the inset SEM image; (c) Size distribution of the LNMO sample measured by DLS showing a D_{50} size of 16.8 μm.

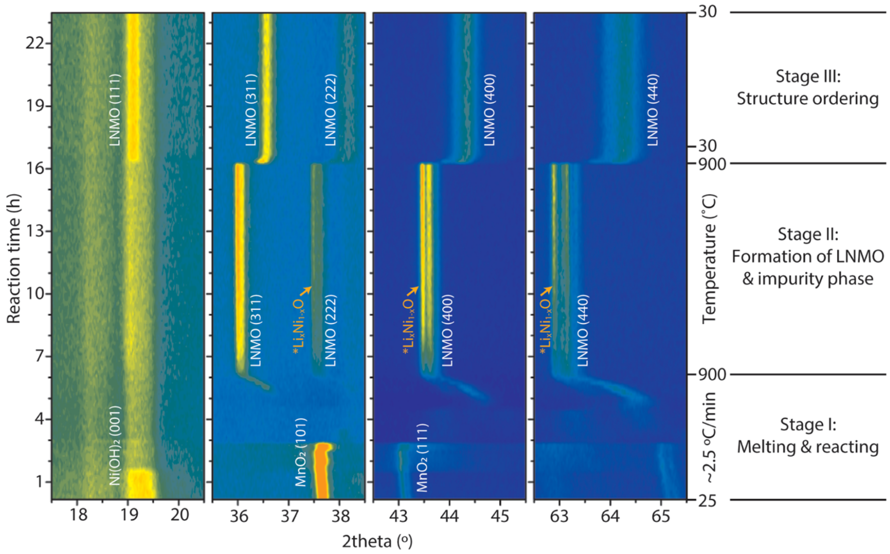

Figure 2. *In situ* XRD studies of the preparation process of LNMO. The *in situ* XRD patterns were recorded at ~10 min interval during the synthesis of large-size single-crystal LNMO particles using LiOH, $Ni(OH)_2$, and MnO_2 as precursors and Li_2MoO_4 as the salt. The materials were heated from 25 to 900 °C at a ramping rate of 2.5 °C min^{-1}, then held at 900 °C for 10 h, and finally allowed to cool down naturally.

°C. The half-cells were cycled at 0.1 C for three cycles before cycling at 0.5 C (1 C = 147 mA g^{-1}) or the rate performance test.

■ RESULTS AND DISCUSSION

Preparation of Large-Size Single-Crystal LNMO Particles. We prepared the single-crystal LNMO samples using stoichiometric amount of LiOH, $Ni(OH)_2$, MnO_2 (mole ratio = 1:0.5:1.5) as precursors and Li_2MoO_4 (melting point at 705 °C) as the molten salt at 950 °C (Figure 1a; see experimental details in Methods). The salt-to-reactant molar ratio $\boldsymbol{R}$ [$\boldsymbol{n}(Li_2MoO_4)/\boldsymbol{n}(LiOH + Ni(OH)_2 + MnO_2) = 0.083$] was significantly smaller in our synthesis than those previously reported ($\boldsymbol{R} \geq 4$),[9,16,18] which lowers the chemical cost of the preparation method and facilitates the separation of the LNMO product from the salts *via* water wash. In our method, molten Li_2MoO_4 functions as the medium of ion diffusion and reaction. Without Li_2MoO_4, large-size single-crystal-like LNMO particles could not be formed (Figure S1). However, Li_2MoO_4 was not a reactant to provide Li^+ because LNMO cannot be made without LiOH. The LNMO sample was separated from Li_2MoO_4 salt by water-washing after the synthesis. After water-washing, Mo could not be detected in the LNMO particles by EDX analysis (Figure 1b). Because the detection limit for SEM−EDX is ~0.5−1.0 atm.%, we further carried out induced couple plasma-optical emission spectroscopy (ICP-OES) measurements on three different batches of samples and found that the Mo content was below 200 ppm. Therefore, we suggest that Mo was likely not doped into the lattice of LNMO. The size distribution of the as-made LNMO particles was measured by dynamic light scattering (DLS), which yielded a D_{50} size of 16.8 μm (Figure 1c). The as-made LNMO particles are significantly larger in grain size compared to those in literature (<10 μm).[9,10,14,18] As a result, a tap density of 2.52 g cm^{-3} was achieved (LNMO density: 4.45 g cm^{-3}), which is quite high and thus favorable for achieving high volumetric energy density.

We have also tried using Li_2SO_4, LiCl, or Li_2WO_4 as the molten salt to prepare single-crystal LNMO particles. The SEM images of the resulting products are shown in Figure S2. Aggregated particles were formed when Li_2SO_4 or LiCl was used. The particles were also smaller in size compared with those made in molten Li_2MoO_4 (Figure 1a). When Li_2WO_4 was used, the sample clearly contained impurity phases because a different contrast was observed in the SEM image. Elemental analysis using ICP-OES indicated that ~9.7 wt % of W was present in the particles made in molten Li_2WO_4. It appears that molten Li_2MoO_4 is unique and promotes the formation of large-size single-crystal LNMO particles, which may be understood using Lewis acid-base theory. MoO_4^{2-} is a stronger Lewis base compared with SO_4^{2-} or Cl^-. We speculate that MoO_4^{2-} interacts more strongly with Ni^{2+} and Mn^{4+} (both are Lewis acids) in the molten salt and promotes their dissolution and mixing to grow larger-size crystal-like particles via the "dissolution-precipitation" mechanism.[36]

In Situ XRD Studies of the Preparation Process of LNMO. After the method to prepare large-size single-crystal LNMO particles was established, we focused our efforts on controlling the phase purity of LNMO. *In situ* XRD studies were carried out to track the phase transitions during the molten-salt-assisted synthesis (Figure 2). All the precursors and Li_2MoO_4 salt were mixed, loaded onto a ceramic stage, and then heated in room temperature to 900 °C at a ramping rate of ~2.5 °C min^{-1}. The reaction temperature was held at 900 °C for 10 h. After that, the system was naturally cooled from 900 °C to 30 °C in ~1 h (because our instrument could not control the cooling rate). XRD patterns were recorded at ~10 min interval. The data are shown using the two-dimensional contour plot, in which the color scale represents the intensity of the XRD signal.

The preparation process can be divided into three stages. In stage I, we observed that the (001) peak of $Ni(OH)_2$ disappeared at ~250 °C, which is likely because of loss of water and long-range ordering. The (101) and (111) peaks of MnO_2 disappeared at ~550 °C, just above its melting point (535 °C). We found it difficult to see the peaks from LiOH and Li_2MoO_4 in this experiment, likely because there were more $Ni(OH)_2$ and MnO_2 by weight in the mix. When the temperature reached ~900 °C, the reaction entered stage II. Concurrent formation of the spinel LNMO phase and the rock-salt impurity phase was observed. The impurity peaks became stronger in intensity as the temperature-holding time increased. We also noticed that the (111) peak of LNMO was almost invisible at 900 °C. This was also observed by A.R. West et al. in *ex situ* XRD patterns of LNMO samples quenched from temperatures above 918 °C.[30] At these temperatures, LNMO was highly oxygen-deficient ($\delta \approx 0.7$ according to A.R. West et al.)[28] and likely had a Li/Ni/Mn stoichiometry deviating from 1:0.5:1.5. In Stage III, the sample was rapidly cooled. The peaks shifted to higher 2θ angles because of thermal contraction. We also observed that the quick emergence of the (111) peak of LNMO and disappearance of the rock-salt impurity peaks confirmed that the LNMO sample became ordered upon cooling.

To study how the cooling rate affects the structural ordering process (which could not be done by our *in situ* XRD instrument), we collected *ex situ* XRD patterns from samples heated in the same way but cooled at different rates (0.8, 2.5, and ~10 °C min^{-1}, respectively). The XRD patterns look quite similar, and all of them can be indexed to a spinel phase (Figure 3a). The XRD technique cannot distinguish the $Fd\bar{3}m$ and $P4_332$ LNMO because of similar X-ray scattering factors of Ni and Mn. Raman spectroscopy is a more suitable tool, which will be discussed in a later section. In terms of the rock-salt impurity phase, its peaks (denoted by black arrows in the XRD pattern for S2) were very weak regardless of the cooling rate. The peaks were hardly visible in sample S1 and S3 even when the XRD patterns were magnified (Figure 3b). This is somewhat surprising to us—one would assume that the rapid-cooled sample (i.e., S3) should contain much more impurities because the oxygen uptake and phase transition processes are considered to be slow according to previous studies.[19,30] Because the X-rays can be absorbed by the solid materials and the beam intensity decreases exponentially with increasing X-ray travel distance (Cu Kα X-ray penetration depth is ~6 μm at 2θ = 36° for LNMO), we suspected that the rock-salt impurity phase and some other subtle structural differences at the interior of the large-sized LNMO particles (D_{50} = 16.8 μm) were likely not captured, which inspired us to carry out the single-particle analysis on the cross-section of the LNMO particles.

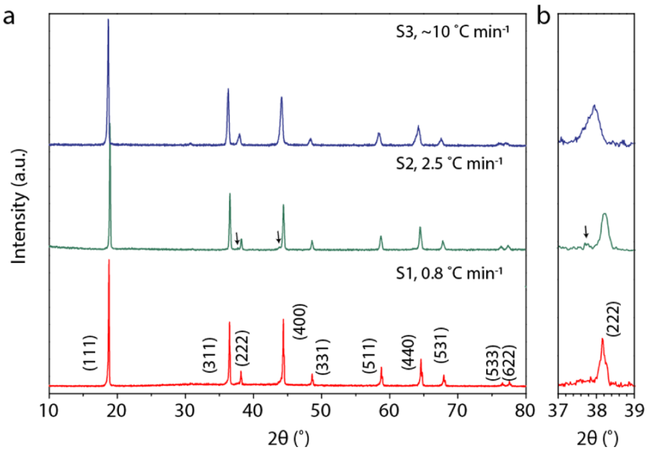

Figure 3. (a) *Ex situ* XRD patterns of LNMO samples. The samples were synthesized via the molten-salt assisted method. They were heated at 950 °C for 8 h in air and then cooled at different rates. Black arrows indicate the peaks associated with the rock-salt impurity phase. Panel (b) is a magnified view of XRD patterns in the range of 37 to 39° of 2θ angles.

Correlative SEM-Raman Studies of the LNMO Samples. To understand the disorder-order phase transition upon cooling and its correlations with the cooling rate at the single-particle level, we first used ion-milling to prepare smooth cross sections of LNMO particles of the three samples (Figure 4a−c, sample S1 to S3) and then carried out correlative SEM-

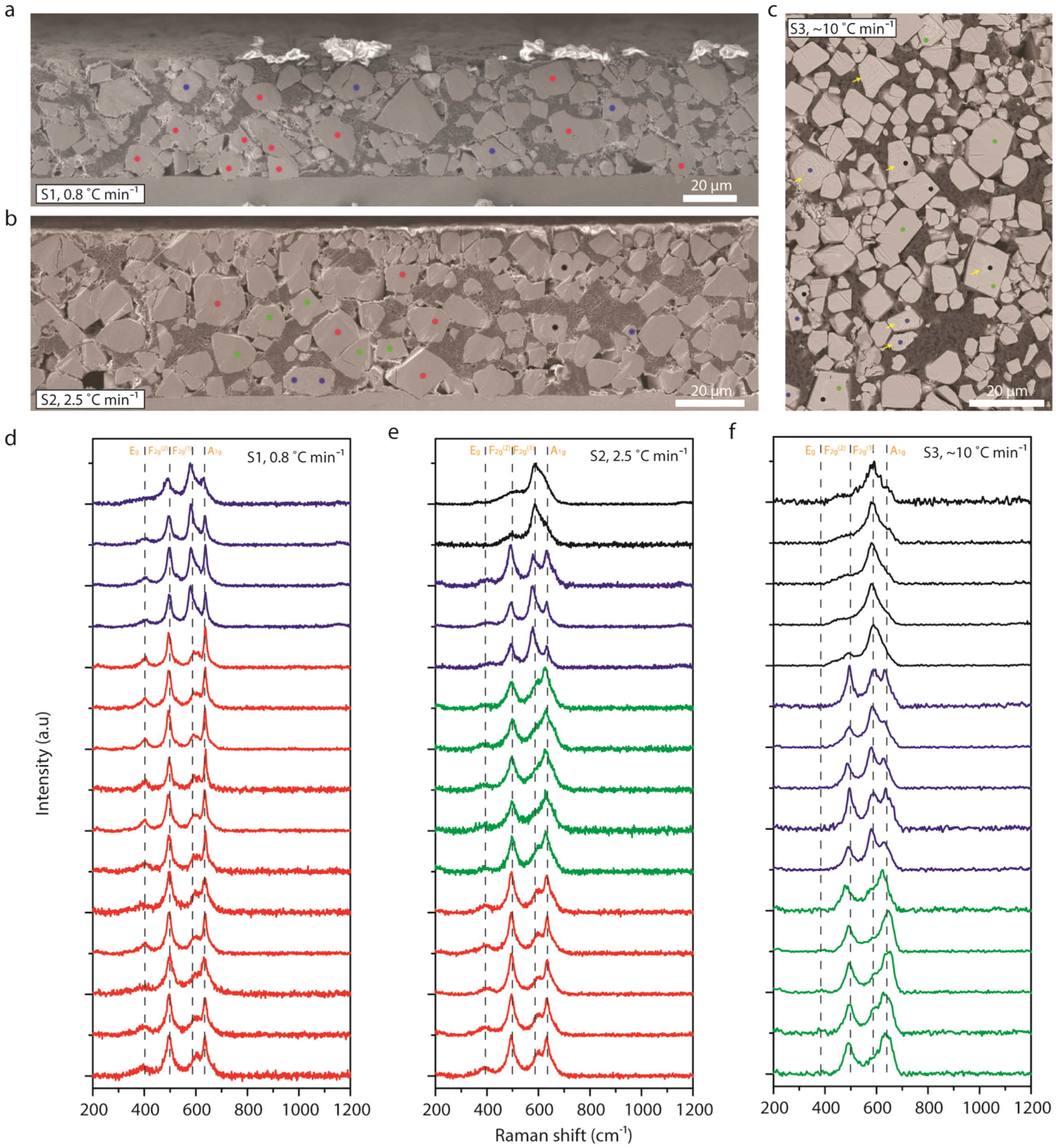

Figure 4. Correlative SEM-Raman studies of the LNMO samples. (a−c) Cross-sectional SEM images of three LNMO samples synthesized in molten Li_2MoO_4 at 950 °C and cooled at 0.8, 2.5, and ~10 °C min^{-1} (natural cooling), respectively. The colored circles indicate the randomly-selected location where the single-point of Raman spectrum was collected. The spectra are shown in (d−f), respectively. Four different characteristic types of Raman spectra are observed and shown in different colors.

Raman studies (Figure 4d−f). We collected single-point Raman spectra from 15 randomly selected particles in sample S1 (cooling rate = 0.8 °C min^{-1}), S2 (2.5 °C min^{-1}), and S3 (~10 °C min^{-1}), respectively. The red, green, blue, and black circles in Figure 4a−c indicate where the single-point Raman spectra were collected. Four different characteristic types of Raman spectra were observed; two in S1 (Figure 4d), four in S2 (Figure 4e), and three in S3 (Figure 4f). The red-colored spectra all exhibit a sharp peak at ~638 cm^{-1}, a smaller peak at ~407 cm^{-1}, and smaller peaks around 590−610 cm^{-1}, which are characteristics of the $P4_332$ LNMO (i.e., the ordered phase) according to previous studies.[21,37] In the green-colored spectra, by contrast, the peaks at ~638 cm^{-1} are weaker and broader, which indicates the presence of the $Fd\bar{3}m$ LNMO (i.e., the disordered phase).[21,37] To the best of our knowledge, the blue- and black-colored Raman spectra have never been reported for LNMO samples in the literature. They are clearly different from those reported for $P4_332$ and $Fd\bar{3}m$ LNMOs (red and green-colored spectra). A close inspection revealed that a blue-colored spectrum could be fitted to a linear combination of the red-colored (or green-colored) spectra and black-colored spectra (Figure S3). Then, the remaining question was to identify the phase that gives rise to the black-colored spectrum.

Interestingly, we noticed that the black spectra were collected from particles showing unique features—different contrasts were observed by SEM (indicated by yellow arrows in Figure 4c). We focused our efforts on one particle with a “white mark” at the center (Figure 5a) and performed correlative Raman and EDX analysis using the same SEM platform (Figure 5b). Single-point Raman spectra were first collected from two regions: one from the “white-mark” area

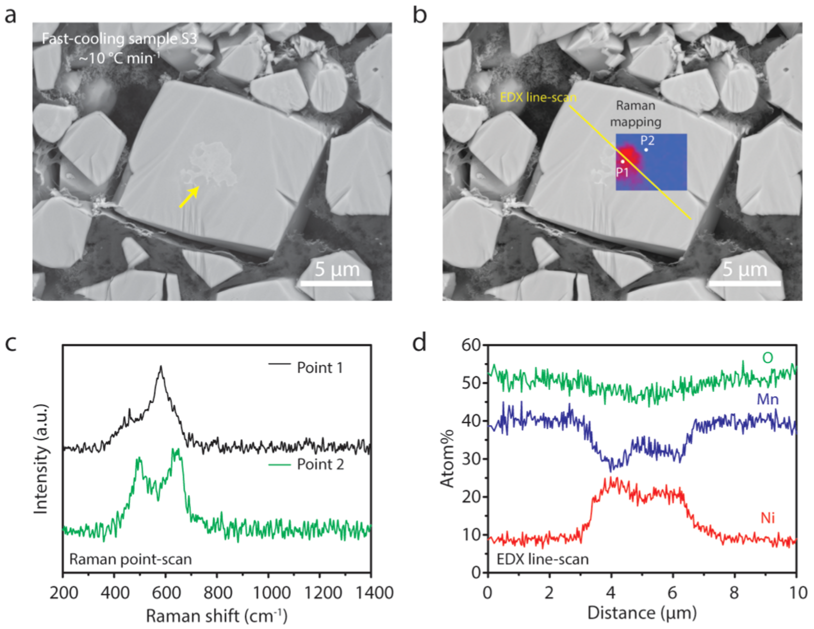

Figure 5. Correlative SEM-Raman-EDX analysis of an LNMO particle. (a) Cross-sectional SEM image of a rapid-cooled (~10 °C min^{-1}) LNMO particle showing a "white mark" at its center; (b) positions of the Raman point-scan, Raman Mapping, and EDX line analysis; (c) Raman spectra collected from point 1 and point 2 shown in panel (b); (d) EDX line-scan results showing Ni-rich region at the center of the particle.

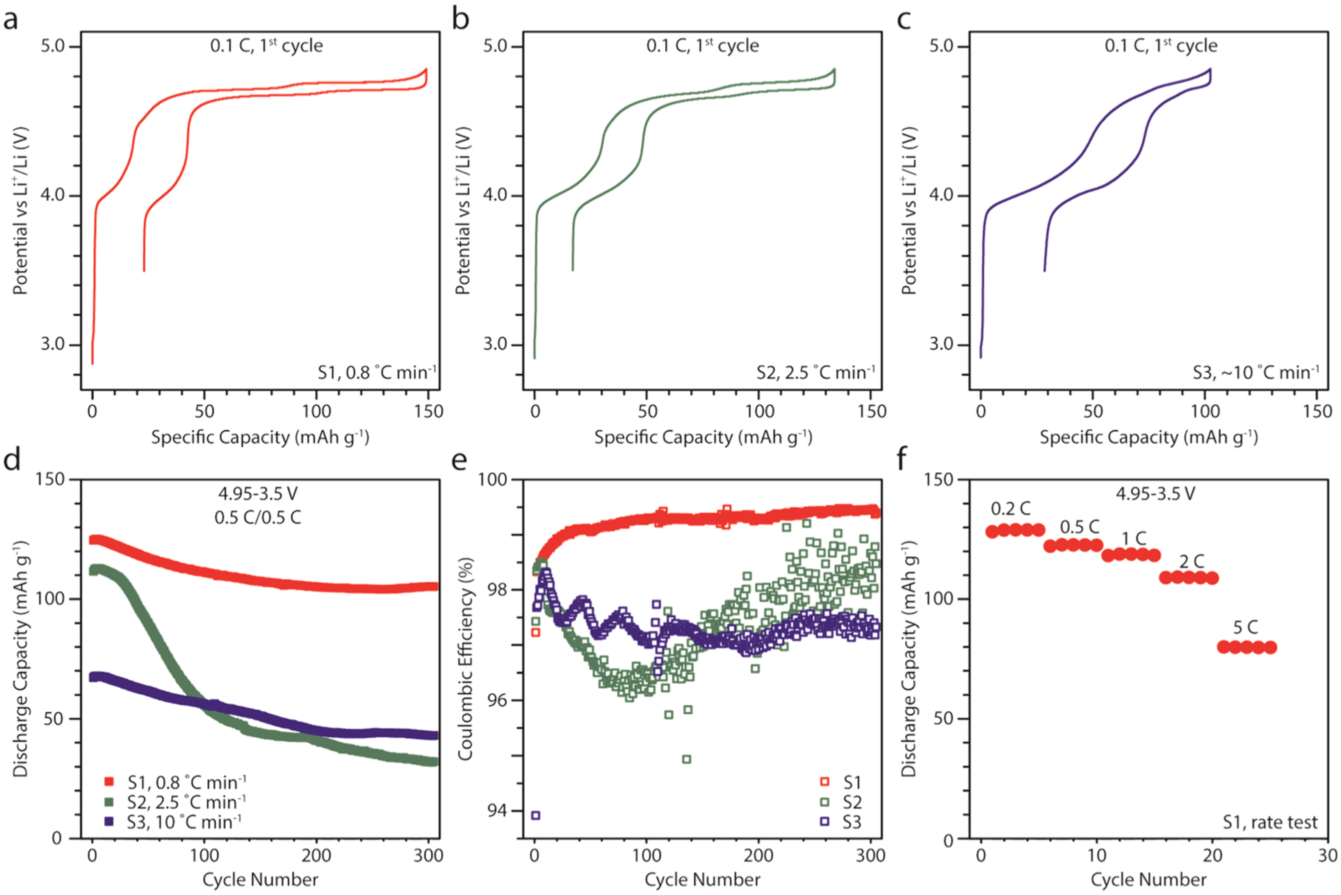

Figure 6. Electrochemical measurements of LNMO samples. (a−c) voltage vs specific capacity curves of the three LNMO samples cooled at different rates; (d,e) cycle performance and Coulombic efficiency of the three LNMO samples during 0.5 C/0.5 C charge−discharge cycling between 4.95 and 3.5 V; (f) Rate performance of LNMO sample S1.

(Point 1), the other from a location away from that area (Point 2). As shown in Figure 5c, the Raman spectrum from Point 1 was indeed the same as those black-colored spectra, as shown in Figure 4e,f, while the one from Point 2 showed similar characteristics to those green-colored spectra and should be from the $Fd\overline{3}m$ LNMO. The spatial distribution of the two phase could be further visualized via Raman mapping (Figure 5b). To determine the chemical composition at the "white mark" region, the EDX line scan was carried out, which revealed the presence of a Ni-rich phase at the center of the particle. We suggest that the "mysterious" phase is a Ni-rich rock-salt (i.e., $Li_xNi_{1-x}O$), which is reasonable because its Raman spectrum (Figure 5c, Point 1) also shows similar characteristics to those observed in rock-salt NiO as reported in ref 38.

We can now turn back and discuss the correlation between phase transition and cooling rate. Rapid-cooled sample S3 was least "perfect". It contained the disordered $Fd\overline{3}m$ LNMO phase and the rock-salt impurity phase (Figure 4f). Decreasing the cooling rate allowed the samples to become more ordered and contained a less rock-salt impurity phase, as observed in samples S2 and S1 (Figure 4d,e). Slow cooling provided more time for oxygen uptake and reduced the formation of oxygen vacancy and Mn^{3+} in the LNMO lattice. The rock-salt impurity phase ($Li_xNi_{1-x}O$) could be converted back to spinel LNMO according the following chemical equation

$$LiNi_{0.5}Mn_{1.5}O_4 \leftrightarrow qLi_xNi_{1-x}O + rLiNi_{0.5-w}Mn_{1.5+w}O_4 + sO_2$$

Such effect has also been discussed in several previous reports.[14,30,39,40] S1 was the most ordered LNMO sample with the least amount of rock-salt impurity among the three samples. The correlative SEM-Raman studies made on the cross-section of particles provide a powerful tool to study structural changes occurring at the interior of particles, which are difficult for conventional bulk-techniques such as XRD. This measurement is not possible for a confocal Raman microscope[41] either because the "white mark" observed by SEM would not be visible under the optical microscope. Compared with the previous studies,[14,30,39,40] this work provides new insights into the location of the rock-salt impurity phase (at the interior of individual LNMO particles) and the single-particle level understanding of the disorder-order transition during cooling.

Electrochemical Performance of the LNMO Samples. Finally, to study how phase purity influences electrochemical performance, S1, S2, and S3 powders were made into electrodes and tested in half-cells using Li metal foils as counter electrodes and 1 M $LiPF_6$ ethylene carbonate-dimethyl carbonate (EC-EMC, 3/7 by weight) as the electrolyte. Figure 6a−c shows the first-cycle charge−discharge voltage profiles of S1, S2, and S3 electrodes at a current density of 0.1 C (1 C = 147 mA g^{-1}) in the voltage range of 4.85−3.5 V (vs Li^+/Li), respectively. All three samples exhibited two voltage plateaus: one at ~4.7 V and the other one at ~4.1 V. It has been reported that the Ni/Mn-ordered $P4_332$ phase exhibits a single voltage plateau at ~4.7 V because of Ni^{2+}/Ni^{4+} redox and the presence of the Ni/Mn disordered $Fd\overline{3}m$ phase leads to an additional voltage plateau at ~4.1 V because of Mn^{3+}/Mn^{4+} redox.[9] In S1, S2, and S3, the Mn^{3+}/Mn^{4+} plateau became shorter with increasing structural ordering (S1 > S2 > S3) enabled by slower cooling. Cyclic voltammograms were also collected from the three samples to show the Mn^{3+}/Mn^{4+}, Ni^{2+}/Ni^{3+}, and Ni^{3+}/Ni^{4+} redox reactions more clearly (Figure S4). To have maximum output energy density, the $P4_332$ phase is preferred. However, a small degree of Ni/Mn disordering ($Fd\overline{3}m$ phase) has been shown to enhance cycle performance and rate capability by inducing solid-solution behaviors during (de)lithiation.[42] S1 appears to be the most ordered sample among the three but still contains a small degree of Ni/Mn disordering based on the correlative SEM-Raman studies (Figure 4d) and the first cycle voltage profile (Figure 6a). It indeed exhibited good electrochemical performance by delivering an initial discharge capacity of 130 mA h g^{-1}, which was higher than S2 (117 mA h g^{-1}, Figure 6b) and S3 (67 mA h g^{-1}, Figure 6c). Upon cycling at 0.5 C (Figure 6d), S1 exhibited remarkable cycle stability by retaining ~85% of its initial capacity after 300 cycles, which was far better than S2 and S3 and among the best reported for LNMO.[14] It also showed higher Coulombic efficiency (Figure 6e), which suggested less side reaction with the liquid electrolyte for S1. The lower Coulombic efficiencies of S2 and S3 (Figure 6e) might be caused by more severe Mn^{3+} dissolution and its subsequent disproportionation to Mn^{2+} and Mn^{4+}, as they showed longer Mn^{3+}/Mn^{4+} plateaus (Figure 6b,c). The Mn dissolution has been reported to cause impedance growth and capacity decay.[11] We also tested the rate capability of S1, which delivered a discharge capacity of 108 mA h g^{-1} at 2 C and 80 mA h g^{-1} at 5 C (Figure 6d). We consider this rate performance acceptable for a sample with such a large particle size (D_{50} = 16.8 μm). These results confirm that the large-size (i.e., small surface area) single-crystal LNMO particles with a high degree of structural ordering (i.e., phase purity) are favorable for stable cycling without compromising the rate performance too much. We also expect that the cycle performance may be further improved by surface doping/coating strategies[13] or electrolyte engineering.[12,43,44] In addition, the LNMO particle size may be tuned to better balance the need for cycle performance and power capability.

■ CONCLUSIONS

Our results show that molten Li_2MoO_4 promotes the formation of large-size single-crystal LNMO particles. *In situ* XRD studies reveal the structural disorder and formation of the rock-salt impurity phase at high temperature used for the synthesis. Through correlative SEM-Raman and EDX analysis at the single-particle level, we show that the Ni-rich rock-salt impurity phase actually exists at the interior of the large-size LNMO particles, which is difficult to be detected by conventional techniques such as XRD or optical Raman spectroscopy because of limitation in probing depth. We further confirm that slow cooling is the key to increasing structural ordering and enhancing electrochemical performance of LNMO. Beyond LNMO, our results highlight the importance of mechanistic studies into material synthesis using *in situ* and correlative techniques (diffraction, microscopy, spectroscopy, and so on), which provides the basis for designing better materials and more efficient preparation methods.

■ ASSOCIATED CONTENT

Supporting Information

The Supporting Information is available free of charge at https://pubs.acs.org/doi/10.1021/acs.jpcc.0c09313.

SEM image and XRD pattern of the LNMO sample synthesized without molten salts, SEM images of LNMO samples synthesized with Li_2SO_4, LiCl, and Li_2WO_4 as the molten salts, Raman spectra and linear combination fitting, and cyclic voltammograms of samples S1, S2, and S3 (PDF)

AUTHOR INFORMATION

Corresponding Author

Linsen Li − *Department of Chemical Engineering, Shanghai Electrochemical Energy Device Research Center (SEED), Shanghai Jiao Tong University, Shanghai 200240, China;* orcid.org/0000-0002-1105-9070; Email: linsenli@sjtu.edu.cn

Authors

Wei-Na Wang − *Department of Chemical Engineering, Shanghai Electrochemical Energy Device Research Center (SEED), Shanghai Jiao Tong University, Shanghai 200240, China*

Dechao Meng − *Department of Chemical Engineering, Shanghai Electrochemical Energy Device Research Center (SEED), Shanghai Jiao Tong University, Shanghai 200240, China*

Guannan Qian − *Department of Chemical Engineering, Shanghai Electrochemical Energy Device Research Center (SEED), Shanghai Jiao Tong University, Shanghai 200240, China*

Sijie Xie − *Suzhou Institute of Nanotech and Nanobionics (SINANO), Chinese Academy of Sciences, Suzhou, Jiangsu 215123, China*

Yanbin Shen − *Suzhou Institute of Nanotech and Nanobionics (SINANO), Chinese Academy of Sciences, Suzhou, Jiangsu 215123, China;* orcid.org/0000-0002-1278-1137

Liwei Chen − *Suzhou Institute of Nanotech and Nanobionics (SINANO), Chinese Academy of Sciences, Suzhou, Jiangsu 215123, China; In-Situ Center for Physical Sciences, School of Chemistry and Chemical Engineering, Shanghai Jiao Tong University, Shanghai 200240, China*

Xiaomin Li − *Instrumental Analysis Center, Shanghai Jiao Tong University, Shanghai 200240, China*

Qunli Rao − *Instrumental Analysis Center, Shanghai Jiao Tong University, Shanghai 200240, China*

Haiying Che − *Department of Chemical Engineering, Shanghai Electrochemical Energy Device Research Center (SEED), Shanghai Jiao Tong University, Shanghai 200240, China*

Jiabing Liu − *Lava Energy Technology Corporation, Suzhou, Jiangsu 215129, China*

Yu-Shi He − *Department of Chemical Engineering, Shanghai Electrochemical Energy Device Research Center (SEED), Shanghai Jiao Tong University, Shanghai 200240, China;* orcid.org/0000-0001-9971-8474

Zi-Feng Ma − *Department of Chemical Engineering, Shanghai Electrochemical Energy Device Research Center (SEED), Shanghai Jiao Tong University, Shanghai 200240, China;* orcid.org/0000-0001-5002-9766

Complete contact information is available at:
https://pubs.acs.org/10.1021/acs.jpcc.0c09313

Author Contributions

[#]W.-N.W. and D.M.hese authors contribute equally to the work.

Notes

The authors declare no competing financial interest.

ACKNOWLEDGMENTS

This work is supported by the Natural Science Foundation of China (22008154 to L.S.L. and 2167165 to Z.F.M.) and partially by Sinopec (420038-1 to L.S.L.).

REFERENCES

(1) Editorial. Battery revolution to evolution. *Nat. Energy* **2019**, *4*, 893.

(2) Whittingham, M. S. Lithium Batteries and Cathode Materials. *Chem. Rev.* **2004**, *104*, 4271.

(3) Li, M.; Lu, J. Cobalt in Lithium-Ion Batteries. *Science* **2020**, *367*, 979.

(4) Kang, K.; Meng, Y. S.; Bréger, J.; Grey, C. P.; Ceder, G. Electrodes with High Power and High Capacity for Rechargeable Lithium Batteries. *Science* **2006**, *311*, 977.

(5) de Boisse, B. M.; Jang, J.; Okubo, M.; Yamada, A. Cobalt-Free O2-Type Lithium-Rich Layered Oxides. *J. Electrochem. Soc.* **2018**, *165*, A3630.

(6) Li, H.; Cormier, M.; Zhang, N.; Inglis, J.; Li, J.; Dahn, J. R. Is Cobalt Needed in Ni-Rich Positive Electrode Materials for Lithium Ion Batteries? *J. Electrochem. Soc.* **2019**, *166*, A429.

(7) Li, W.; Erickson, E. M.; Manthiram, A. High-Nickel Layered Oxide Cathodes for Lithium-Based Automotive Batteries. *Nat. Energy* **2020**, *5*, 26.

(8) Li, W.; Lee, S.; Manthiram, A. High-Nickel NMA: A Cobalt-Free Alternative to NMC and NCA Cathodes for Lithium-Ion Batteries. *Adv. Mater.* **2020**, *32*, 2002718.

(9) Kim, J.-H.; Myung, S.-T.; Yoon, C. S.; Kang, S. G.; Sun, Y.-K. Comparative Study of LiNi0.5Mn1.5O4-$\delta$and LiNi0.5Mn1.5O4Cathodes Having Two Crystallographic Structures: Fd$\bar{3}$mandP4332. *Chem. Mater.* **2004**, *16*, 906.

(10) Ma, X.; Kang, B.; Ceder, G. High Rate Micron-Sized Ordered LiNi[sub 0.5]Mn[sub 1.5]O[sub 4]. *J. Electrochem. Soc.* **2010**, *157*, A925.

(11) Manthiram, A.; Chemelewski, K.; Lee, E.-S. A perspective on the high-voltage LiMn1.5Ni0.5O4 spinel cathode for lithium-ion batteries. *Energy Environ. Sci.* **2014**, *7*, 1339.

(12) Xu, H.; Zhang, H.; Ma, J.; Xu, G.; Dong, T.; Chen, J.; Cui, G. Overcoming the Challenges of 5 V Spinel LiNi0.5Mn1.5O4 Cathodes with Solid Polymer Electrolytes. *Energy Environ. Sci.* **2019**, *4*, 2871.

(13) Piao, J.-Y.; Sun, Y.-G.; Duan, S.-Y.; Cao, A.-M.; Wang, X.-L.; Xiao, R.-J.; Yu, X.-Q.; Gong, Y.; Gu, L.; Li, Y.; et al. Stabilizing Cathode Materials of Lithium-Ion Batteries by Controlling Interstitial Sites on the Surface. *Chem* **2018**, *4*, 1685.

(14) Liu, H.; Zhang, X.; He, X.; Senyshyn, A.; Wilken, A.; Zhou, D.; Fromm, O.; Niehoff, P.; Yan, B.; Li, J.; et al. Truncated Octahedral High-Voltage Spinel LiNi0.5Mn1.5O4Cathode Materials for Lithium Ion Batteries: Positive Influences of Ni/Mn Disordering and Oxygen Vacancies. *J. Electrochem. Soc.* **2018**, *165*, A1886.

(15) Chen, B.; Ben, L.; Chen, Y.; Yu, H.; Zhang, H.; Zhao, W.; Huang, X. Understanding the Formation of the Truncated Morphology of High-Voltage Spinel LiNi0.5Mn1.5O4 via Direct Atomic-Level Structural Observations. *Chem. Mater.* **2018**, *30*, 2174.

(16) Kuppan, S.; Xu, Y.; Liu, Y.; Chen, G. Phase Transformation Mechanism in Lithium Manganese Nickel Oxide Revealed by Single-Crystal Hard X-Ray Microscopy. *Nat. Commun.* **2017**, *8*, 14309.

(17) Zhang, X.; Cheng, F.; Yang, J.; Chen, J. LiNi0.5Mn1.5O4 Porous Nanorods as High-Rate and Long-Life Cathodes for Li-Ion Batteries. *Nano Lett.* **2013**, *13*, 2822.

(18) Hai, B.; Shukla, A. K.; Duncan, H.; Chen, G. The effect of particle surface facets on the kinetic properties of LiMn1.5Ni0.5O4-cathode materials. *J. Mater. Chem. A* **2013**, *1*, 759.

(19) Cai, L.; Liu, Z.; An, K.; Liang, C. Unraveling structural evolution of LiNi0.5Mn1.5O4 by in situ neutron diffraction. *J. Mater. Chem. A* **2013**, *1*, 6908.

(20) Cabana, J.; Casas-Cabanas, M.; Omenya, F. O.; Chernova, N. A.; Zeng, D.; Whittingham, M. S.; Grey, C. P. Composition-Structure

Relationships in the Li-Ion Battery Electrode Material LiNi0.5Mn1.5O4. *Chem. Mater.* **2012**, *24*, 2952.

(21) Wang, L.; Li, H.; Huang, X.; Baudrin, E. A comparative study of Fd-3m and P4332 "LiNi0.5Mn1.5O4". *Solid State Ionics* **2011**, *193*, 32.

(22) Xue, Y.; Han, Y.; Yu, H.-X.; Shu, J.; Wang, Z.-B.; Zheng, L.-L.; Xia, Y.-F. Improving Rate Performance of High-Voltage Spinel Cathode by Changing Structural Evolution from Two-Phase to Solid-Solution Reactions. *Electrochim. Acta* **2018**, *281*, 24.

(23) Han, Y.; Xue, Y.; Xia, Y.-F.; Zhang, J.-N.; Yu, F.-D.; Gu, D.-M.; Wang, Z.-B. Design of synergistic-coated layer of La2O3/Al2O3 in LiNi0.5Mn1.5O4 cathode for enhanced cycling stability and rate capability. *Ionics* **2019**, *25*, 2459.

(24) Jung, R.; Metzger, M.; Maglia, F.; Stinner, C.; Gasteiger, H. A. Oxygen Release and Its Effect on the Cycling Stability of LiNixMnyCozO2(NMC) Cathode Materials for Li-Ion Batteries. *J. Electrochem. Soc.* **2017**, *164*, A1361.

(25) Harlow, J. E.; Ma, X.; Li, J.; Logan, E.; Liu, Y.; Zhang, N.; Ma, L.; Glazier, S. L.; Cormier, M. M. E.; Genovese, M.; et al. A Wide Range of Testing Results on an Excellent Lithium-Ion Cell Chemistry to be used as Benchmarks for New Battery Technologies. *J. Electrochem. Soc.* **2019**, *166*, A3031.

(26) Qian, G.; Zhang, Y.; Li, L.; Zhang, R.; Xu, J.; Cheng, Z.; Xie, S.; Wang, H.; Rao, Q.; He, Y.; et al. Single-Crystal Nickel-Rich Layered-Oxide Battery Cathode Materials: Synthesis, Electrochemistry, and Intra-Granular Fracture. *Energy Storage Mater.* **2020**, *27*, 140.

(27) Liu, W.; Oh, P.; Liu, X.; Lee, M.-J.; Cho, W.; Chae, S.; Kim, Y.; Cho, J. Nickel-Rich Layered Lithium Transition-Metal Oxide for High-Energy Lithium-Ion Batteries. *Angew. Chem., Int. Ed.* **2015**, *54*, 4440.

(28) Woodford, W. H.; Carter, W. C.; Chiang, Y.-M. Design Criteria for Electrochemical Shock Resistant Battery Electrodes. *Energy Environ. Sci.* **2012**, *5*, 8014.

(29) Chen, Y.; Sun, Y.; Huang, X. Origin of the Ni/Mn ordering in high-voltage spinel LiNi0.5Mn1.5O4: The role of oxygen vacancies and cation doping. *Comput. Mater. Sci.* **2016**, *115*, 109.

(30) Pasero, D.; Reeves, N.; Pralong, V.; West, A. R. Oxygen Nonstoichiometry and Phase Transitions in LiMn[sub 1.5]Ni[sub 0.5]O[sub 4−δ]. *J. Electrochem. Soc.* **2008**, *155*, A282.

(31) Schmidt, U.; Unger, A.-K.; Eder, M., Hollricher, O.. Charaterizing 2D Materials with RISE Microscopy. https://www.witec.de/assets/Literature/Files/AppNote-ZEISS-RISE.pdf (accessed 22 August 2020).

(32) Wille, G.; Lahondere, D.; Schmidt, U.; Duron, J.; Bourrat, X. Coupling SEM-EDS and Confocal Raman-in-SEM Imaging: A New Method for Identification and 3D Morphology of Asbestos-Like Fibers in a Mineral Matrix. *J. Hazard. Mater.* **2019**, *374*, 447.

(33) Setoguchi, M.; Sakamoto, C. Crystal growth of Li2MSiO4 (M = Mg, Zn) by flux method. *J. Cryst. Growth* **1974**, *24-25*, 674.

(34) Kimijima, T.; Zettsu, N.; Yubuta, K.; Hirata, K.; Kami, K.; Teshima, K. Molybdate flux growth of idiomorphic Li(Ni1/3Co1/3Mn1/3)O2 single crystals and characterization of their capabilities as cathode materials for lithium-ion batteries. *J. Mater. Chem. A* **2016**, *4*, 7289.

(35) Flynn, S.; Sanghvi, S.; Nisbet, M. L.; Griffith, K. J.; Zhang, W.; Halasyamani, P. S.; Haile, S. M.; Poeppelmeier, K. R. LiIn2SbO6: A New Rutile-Related Structure Type with Unique Ion Channels. *Chem. Mater.* **2020**, *32*, 4785.

(36) Li, Z.; Lee, W. E.; Zhang, S. Low-Temperature Synthesis of CaZrO3Powder from Molten Salts. *J. Am. Ceram. Soc.* **2007**, *90*, 364.

(37) Jehnichen, P.; Korte, C. Operando Raman Spectroscopy Measurements of a High-Voltage Cathode Material for Lithium-Ion Batteries. *Anal. Chem.* **2019**, *91*, 8054.

(38) Mironova-Ulmane, N.; Kuzmin, A.; Steins, I.; Grabis, J.; Sildos, I.; Pärs, M. Raman Scattering in Nanosized Nickel Oxide NiO. *J. Phys. Conf.* **2007**, *93*, 012039.

(39) Lee, E.-S.; Nam, K.-W.; Hu, E.; Manthiram, A. Influence of Cation Ordering and Lattice Distortion on the Charge-Discharge Behavior of LiMn1.5Ni0.5O4 Spinel between 5.0 and 2.0 V. *Chem. Mater.* **2012**, *24*, 3610.

(40) Zhong, Q.; Bonakdarpour, A.; Zhang, M.; Gao, Y.; Dahn, J. R. Synthesis and Electrochemistry of LiNi x Mn2 − x O 4. *J. Electrochem. Soc.* **1997**, *144*, 205.

(41) Gilbert, J. A.; Maroni, V. A.; Cui, Y.; Gosztola, D. J.; Miller, D. J.; Abraham, D. P. Composition and Impedance Heterogeneity in Oxide Electrode Cross-Sections Detected by Raman Spectroscopy. *Adv. Mater. Interfaces* **2018**, *5*, 1701447.

(42) Lee, J.; Kim, C.; Kang, B. High electrochemical performance of high-voltage LiNi0.5Mn1.5O4 by decoupling the Ni/Mn disordering from the presence of Mn3+ ions. *NPG Asia Mater.* **2015**, *7*, No. e211.

(43) Wang, J.; Yamada, Y.; Sodeyama, K.; Chiang, C. H.; Tateyama, Y.; Yamada, A. Superconcentrated Electrolytes for a High-Voltage Lithium-Ion Battery. *Nat. Commun.* **2016**, *7*, 12032.

(44) Li, S. R.; Sinha, N. N.; Chen, C. H.; Xu, K.; Dahn, J. R. A Consideration of Electrolyte Additives for LiNi0.5Mn1.5O4/Li4Ti5O12Li-Ion Cells. *J. Electrochem. Soc.* **2013**, *160*, A2014.